Materiales de Construcción
Vol. 74, Issue 354, April-June 2024, e342
ISSN-L: 0465-2746
https://doi.org/10.3989/mc.2024.367923

Design of an explicit crack bridging constitutive model for engineered cementitious composites using polyvinyl alcohol (PVA) or polyethylene (PE) fiber

Z. Wang, B. Li✉, L. Li, Z. Zhang

College of Architecture and Environment, Sichuan University, Key Laboratory of Deep Underground Science and Engineering for Ministry of Education, (Chengdu, China)
✉: libix@126.com

Received 14 November 2023
Accepted 28 March 2024
Available on line 11 June 2024

ABSTRACT: This paper aims to establish an explicit crack bridging model that can link engineered cementitious composites (ECC) behavior from single fiber to single crack scale, which is great of designing ECC featuring pseudo tensile strain hardening and multiple cracks expanding by tailoring microstructure and materials selection. In this study, fiber bridging stress was divided into three parts including fiber bridging stress with no rupture, fiber debonding fracture stress, and fiber pullout fracture stress. Subsequently, the fundamental crack bridging model was emerged when fiber bridging stress with no rupture subtracted from the fiber rupture stress in debonding and pullout stage. Moreover, two-way pullout and Cook-Gordon effect were also considered to establish the complete model. It was found that the two-way pullout situation of polyvinyl alcohol (PVA) fiber has a significant influence on the crack opening width due to its slip hardening property, while the Cook-Gordon effect presents a faint crack width increment for PVA-ECC. However, the Cook-Gordon effect makes a significant contribution to the crack opening width of the composite produced by polyethylene (PE). This building intelligible model presents a better prediction for ECC through the comparison of experimental data or real average crack width in previous models, thus confirming the validity of this model.

KEY WORDS: Engineered cementitious composites; Crack bridging model; Two-way pullout; Fiber pullout rupture.

Citation/Citar como: Z Wang, B Li, L Li, Z Zhang. 2024. Design of an explicit crack bridging constitutive model for engineered cementitious composites using polyvinyl alcohol (PVA) or polyethylene (PE) fiber. Mater. Construcc. 74(354):e342. https://doi.org/10.3989/mc.2024.367923.

RESUMEN: *Diseño de un modelo constitutivo explícito de formación de fisuras para compuestos cementicios diseñados utilizando fibra de polivinil alcohol (PVA) o de polietileno (PE).* El objetivo de este trabajo es establecer un modelo explícito de formación de fisuras que pueda vincular el comportamiento de los materiales compuestos cementicios de ingeniería (ECC) desde la escala de una sola fibra hasta la de una sola fisura. En este estudio, la tensión de puenteo de la fibra se dividió en tres partes: tensión de puenteo de la fibra sin rotura, tensión de fractura por desprendimiento de la fibra y tensión de fractura por extracción de la fibra. Se descubrió que la situación de extracción bidireccional de la fibra de polivinil alcohol (PVA) tiene una elevada influencia significativa en la anchura de apertura de la fisura, mientas que el efecto Cook-Gordon contribuye de forma significativa a la anchura de apertura de fisura del compuesto fabricado con polietileno (PE). Este modelo de construcción inteligible presenta una mejor predicción para ECC a través de la comparación de datos experimentales o de la anchura media real de la fisura en modelos anteriores, confirmando así su validez.

PALABRAS CLAVE: Compuestos cementicios de ingeniería; Modelo de puenteo de fisuras; Arrancamiento bidireccional; Rotura por arrancamiento de fibras.

Nomenclature			
d_f	Fiber diameter (m)	θ	Inclined angle
L_f	Fiber length (m)	σ_{bb}	Fiber bridging stress during debonding periods (Pa)
V_f	Fiber volume fraction	σ_{bp}	Fiber bridging stress during slipping periods (Pa)
E_f	Fiber modulus of elasticity (Pa)	$l_d(\delta)$	Current debonding ruptured length (m)
E_m	Elastic modulus of the matrix (Pa)	δ^*	Crack opening width when fibers are fully debonding (m)
β	Slip hardening coefficient	$L_d(\theta)$	Critical debonding embedment length (m)
f'	Fiber tensile strength reduction coefficient	$L_p(\theta)$	Critical slipping embedment length (m)
f	Snubbing coefficient	$l_p(\delta)$	Current slipping ruptured length (m)
σ_{fu}	Fiber tensile fracture strength (Pa)	θ_c	Inclined angle when intersects with $L_d(\theta)$
σ_c	Matrix tensile cracking stress (Pa)	θ_d	Inclined angle when $L_f/2$ intersects with $L_d(\theta)$
Le	Fiber embedment length (m)	σ_b	Nominal fiber bridging stress (Pa)
L_L	Fiber embedment length of long end (m)	ξ_b	Efficiency of fibers bridging
Ls	Fiber embedment length of short end (m)	α	Cook-Gordon parameter
τ_0	Matrix/fiber frictional stress (Pa)	δ_{cg}	Fiber stretch segment according to Cook-Gordon effect
G_d	Chemical bond stress (Pa)	σ_c	Matrix tensile cracking stress in
σ_0	Peak fiber bridging stress in	J_{tip}	Crack tip toughness
J_b'	Complementary energy	z	Centroid distance
δ_r	Remedial crack opening width		

1. INTRODUCTION

Fibers with characters of high elastic modulus, high elongation rate, and high ultimate tensile strength are usually used to overcome the crack sensibility and intrinsic brittleness of concrete (1, 2). ECC composited by PE or PVA, cement, and fine aggregates exhibit an applausive tensile pseudo strain hardening property, meanwhile, multiple tight cracking with a mean crack width under 100 μm was usually accompanied in the tensile plane (3-6). In addition, the fiber-reinforced concrete containing polyolefin and steel fibers also could exhibit great toughness and crack resistance if the fibers achieve a suitable distribution (7-9), while it is difficult to enhance the ductility obtained by the strain hardening and multiple cracks expanding action compared to PE-ECC and PVA-ECC. Hence, the superior tensile properties of ECC contributed to its wide application prospects in infrastructural construction.

On basis of fracture mechanics and micromechanical principles, ECC was designed by linking from single fiber to single crack scale to achieve the tensile pseudo strain hardening properties (10, 11). The crack bridging model of composites expresses the relation of fiber bridging stress versus crack opening distance, which was of primary importance to implement the multiple crack expanding and tensile pseudo strain hardening characters by energy-based criterion and strength-based criterion (12). Hence, tailoring raw microstructure including fiber, matrix, and fiber/matrix by fiber bridging law can capture a superior tensile property of ECC (13, 14). Moreover, modeling the micromechanical fiber bridging stress vs crack opening width relation also could evolve the macroscopic tensile properties of ECC (15, 16).

To date, continuous efforts have been made to establish the crack bridging relation based on the fiber failure models and interface properties. Li et al. (17) first established the fiber pullout model (FPM) which considered the interfacial frictional stress as a constant during the fiber pullout process. Thereafter, Lin et al. (18) introduce the interfacial slip-hardening coefficient to advance the precision of FPM where interfacial frictional strength is enhanced by the increasing fiber pullout distance. However, fiber fracture was neglected in above two models when fiber bridging stress is greater than the fiber apparent tensile strength. Based on FPM, Maalej et al. (19) first considered fiber rupture in debonding process and proposed the fiber pullout rupture model (FPRM). Afterward, Kanda et al. (20) included a chemical bond stress to advance FPRM where the chemical bond stress and interfacial frictional stress control the fiber-matrix interface properties. Thereafter, Lin et al.

(21) further introduced the interfacial slip-hardening coefficient to the above advanced FPRM. Noticeably, fiber bridging stress during pullout stage could exceed the fiber tensile strength due to the slip-hardening character of single fiber (22). However, the situation of fiber rupture in slipping stage was no considered in FPRM and two advanced FPRMs.

In recent years, fiber rupture in slipping stage was gradually introduced to advance the fiber bridging model. Based on the advanced FPRM (21),Yang et al. (23) considered fiber rupture in the debonding and slipping process, matrix micro-spalling, and Cook-Gordon effect to improve the precision accuracy of the fiber bridging model. However, no explicit expression was presented in the model. Yu et al. (24) created the implicit micromechanical modeling of crack-bridging relations of hybrid-fiber strain-hardening cementitious composites considering the interaction between different fibers based on Yang's model. In addition, based on the advanced FPRM, Huang et al. (14) developed an explicit crack bridging model that included fiber rupture in debonding and slipping stage (21), while the fiber two way pullout was explicated in this model. However, the crack opening width at the fiber complete debonding point was neglected in the fiber limiting embedment and bridging stress, while Cook-Gordon effect was also excluded. Cook-Gordon effect presents a premature fiber/matrix interface debonding normal to the fiber axis caused by a tensile stress located ahead of a blunt matrix crack implementing towards a fiber under remote tensile load, which makes fiber debonding take place ahead of the matrix crack, resulting in stretching of a free fiber segment and additional crack opening (23). Thus, excluding Cook-Gordon effect would reduce the crack width and mitigate the prediction accuracy of fiber bridging model. Based on the reviewed fiber bridging model, it is more reasonable to establish an advanced crack bridging model including the overall properties of the fibers, slip-hardening interfacial coefficient, fiber rupture in debonding and slipping stage, Cook-Gordon effect, and fiber two-way pullout.

The main objective of this paper was to establish an explicit fiber bridging model of ECC that could be easily adopted for all ECC researchers. On basis of Lin et al.'s FPRM model (21), the fiber rupture zone in this study in debonding and slipping stage was separately calculated. Then, the fiber bridging model was derived when complete fiber bridging stress with no fracture subtracted the bridging stress in the fiber debonding and slipping zone. In addition, Cook-Gordon effect and fiber two-way pullout were included to modify the crack bridging model, thus evolving the ultimate σ(δ) relation of ECC. Finally, the current σ(δ) relation was verified against experimental fiber bridging behavior in a series of ECCs. This analytical model was expected to favor ECC material design in terms of pseudo strain hardening and multiple crack opening behavior.

2. FIBER BRIDGING THEORY

To obtain pseudo strain hardening and multiple crack expanding behavior of ECC under tensile load, the fiber bridging theory was fundamentally framed based on the energy-based criterion and strength-based criterion (20, 25). The typical σ(δ) relation is shown in Figure 1.

(1) Strength-based criterion

$$\sigma_c \leq \sigma_0 \qquad [1]$$

Where σ_c and σ_0 are the matrix tensile cracking stress and peak fiber bridging stress in σ(δ) curve, respectively. Strength-based criterion is a prerequisite for multiple cracking development, indicating that fiber bridging stress could be effectively transferred from initial crack to the next crack only when the maximum peak fiber bridging stress exceeds the matrix tensile cracking stress depended on the fracture toughness and flaw size of the matrix (26), which control the start-up of cracks.

(2) Energy-based criterion

$$J_{tip} \leq J_b{}' \qquad [2]$$

Where J_{tip} and $J_b{}'$ are the crack tip toughness and complementary energy, respectively. The specific formula of J_{tip} and $J_b{}'$ are shown in Figure 1. Energy-based criterion was derived by the reference (27) using Jintegral analysis, which guides saturated multiple cracking development only if the crack tip toughness is lower than the complementary energy. Moreover, crack tip toughness is approximately equal to the formula K_m^2/E_m, where E_m is tensile elastic modulus. Moreover, matrix cracking can absorb energy in the cracking process, which can affect the stress field intensity factor (KI). With KI increases, the stress at the crack tip is large enough to reach the fracture strength of the material, and the crack will expand and lead to fracture. So, the Km used in this work is the matrix fracture toughness, which is the critical value of KI. The matrix fracture toughness could be obtained by single crack three-point bend test per ASTM E 1820 -05a (28).

Simultaneous requirement of Equation [1] and [2] is indispensable to achieve the characteristics of pseudo strain hardening and multiple cracking of ECC. Both criterions are well employed to guide the materials tailoring to achieve high ductility performances by strain-hardening strength indices ($PSH_{strength} = \sigma_0/\sigma_c$) and strain-hardening energy indices ($PSH_{energy} = J_b{}'/J_{tip}$) (29). For PVA-ECC, the $PSH_{strength}$ and PSH_{energy} should exceed 1.5 and 3, respectively, while that of PE-ECC should greater than 1.2 and 3, respectively (13).

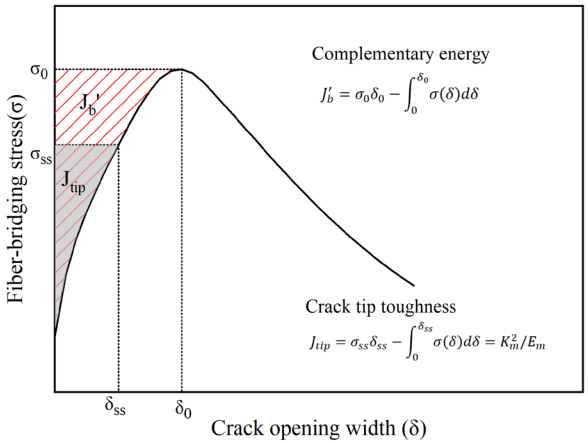

Figure 1. The typical relation of ECC (4).

3. SINGLE FIBER PULLOUT BEHAVIOR

Based on the crack plane, the fiber pullout model was designed during debonding and slipping stage. Figure 2 shows the fiber inclined angle and embedment length scheme, where θ is the inclined angle $\theta \in (0, \frac{\pi}{2})$, L_L *and* L_S are the embedment length of the long end and short end, respectively. δ_{0L} *and* δ_{0S} are the crack opening distance corresponding to the complete debonding point of the long end and short end, respectively. The fiber starts to slip when δ exceeds $2\delta_{0S}$. The composite bridging stress can be computed by summing all single fiber stressing fibers crossing the crack plane (18). The relation between fiber bridging stress and crack opening distance was established, which mainly included fiber, matrix, and fiber-matrix properties, as shown in Equation [3]. Meanwhile, the crack displacement at full-debonding point was defined in Equation [4] (18, 21).

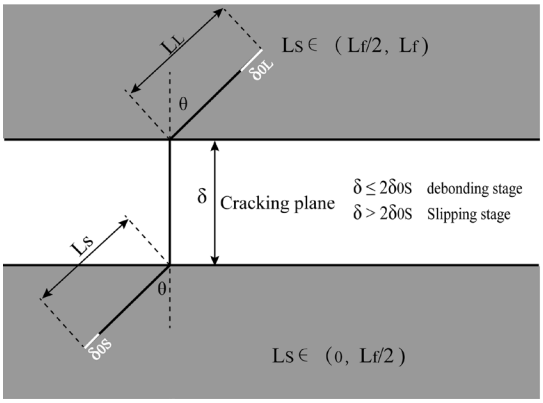

Figure 2. Fiber inclined angle and embedment length schematic diagram.

$$\sigma_b(\delta, L_e, \theta)\begin{cases}\sigma_{bb}(\delta,\theta) = \sqrt{\frac{4E_f(1+\eta)(\delta\tau_0+2G_d)}{d_f}}e^{f'\theta} & 0 \le \delta < 2\delta_0 \\ \sigma_{bp}(\delta, L_e, \theta) = \frac{4\tau_0}{{d_f}^2}(d_f + \beta(\delta - 2\delta_0)(L_e - (\delta - 2\delta_0))e^{f'\theta} & 2\delta_0 \le \delta < L_e\end{cases} \quad [3]$$

$$\delta_0 = \frac{2{L_e}^2\tau_0(1+\eta)}{d_f E_f} + 2\sqrt{\frac{2{L_e}^2 G_d(1+\eta)}{d_f E_f}} \quad [4]$$

Where σ_{bb} and σ_{bp} presents the fiber bridging stress during debonding and slipping periods, respectively. τ_0 is the matrix/fiber frictional stress, G_d is the chemical bond stress, E_f is the modulus of elasticity of fiber, β is the slip hardening coefficient, d_f presents fiber diameter. L_e is the fiber embedment length, which is less than $L_f/2$ Moreover, f is the snubbing coefficient (30). $\eta = V_f E_f/(1 - V_f)E_m$, where V_f is the fiber volume fraction and E_m is the matrix tensile elastic modulus.

Additionally, the fiber apparent tensile strength exhibits a degradation effect, which decreases with the increasing inclined angle (31). For PVA fiber, the strength reduction effect could be accounted by Equation [5].

$$\sigma_{fu}(\theta) = \sigma_{fu}e^{-f'\theta} \quad [5]$$

Where σ_{fu} is fiber tensile fracture strength, f' is the fiber tensile strength reduction coefficient.

4. CRACK BRIDGING MODEL OF ECC

4.1. Averaging fiber bridging stress-crack opening width

Fiber location and orientation are the main factors to influence the σ(δ) relation. According to (7, 32), the σ(δ) model could be accounted by summing single stress from individual bridging fibers considering probability density functions, as shown in Equation [6].

$$\sigma(\delta) = V_f\int_0^{\frac{\pi}{2}}\int_0^{\frac{L_f}{2}\cos\theta}\sigma_b(\delta, z, \theta)p(\theta, z)dzd\theta \quad [6]$$

Where $p(\theta, z)$ is the probability density function of centroid distance z and orientation angle θ, L_f is the fiber length. For a 2D or 3D uniform random distribution, corresponding formulas are defined as follows:

$$p(\theta, z) = p(\theta)p(z) \quad [7]$$

$$p(\theta) = \begin{cases}\frac{2}{\pi} & 2D \\ sin\theta & 3D\end{cases} \quad \left(0 \le \theta \le \frac{\pi}{2}\right) \quad [8]$$

$$p(z) = \frac{2}{L_f} \quad \left(0 \le z \le \frac{L_f}{2}\right) \quad [9]$$

Where V_f is the fiber volume fraction. It is noteworthy that V_f is used with limits since excessive fi-

bers would lead to the agglomeration phenomenon that mitigates the tensile properties and workability. z is the function of embedment length L_e and orientation angle θ. After changing z with $L_e = \frac{L_f}{2} - \frac{z}{cos\theta}$, and replacing the Equation [7-9] into (6), Equation [6] could be changed as follows:

$$\sigma(\delta) = \frac{V_f}{L_f}\int_0^{\frac{\pi}{2}}\int_0^{\frac{L_f}{2}} \sigma_b(\delta, L_e, \theta) sin2\theta dL_e d\theta \quad [10]$$

4.2. No Fiber fractures

Firstly, assuming that all fiber in crack plane would not fracture under axial tensile force, the embedment length $l_d(\delta)$ at full debonding point can be derived when crack opening width δ reaches $2\delta_0$ (21), as shown in Equation [11].

$$l_d(\delta) = \sqrt{\frac{(\tau_0\delta + 2G_d)}{4(1+\eta){\tau_0}^2}} - \sqrt{\frac{E_f d_f G_d}{2(1+\eta){\tau_0}^2}} \quad [11]$$

Figure 3 illustrates the fiber embedment at full debonding point with varying crack opening width. Fibers between δ to $l_d(\delta)$ are in slipping stage, in which fibers between $l_d(\delta)$ to $L_f/2$ are in debonding behavior. Moreover, the crack opening width δ^* can be obtained when fibers having a peak embedment length of $L_f/2$ are in complete debonding point, which is given in Equation [12].

$$\delta^* = 2\delta_0\left(L_e = \frac{L_f}{2}\right) = \frac{\tau_0(1+\eta){L_f}^2}{d_f E_f} + \sqrt{\frac{8G_d(1+\eta){L_f}^2}{d_f E_f}} \quad [12]$$

Hence, Fiber states without fiber rupture could be divided into two kinds, as plotted in Figure 4. The crack opening width could be distinguished into two types according to the value of δ, δ^*, and $L_f/2$. Then, the crack bridging stress with no fibers rupture $\sigma_N(\delta)$ for ECC can be calculated by integrating all contributory fibers bridging stress, which is given in Equation [13].

$$\sigma_N(\delta) = \begin{cases} \frac{V_f}{L_f}\left\{\int_0^{\frac{\pi}{2}}\int_\delta^{l_d(\delta)} \sigma_{bp}(\delta, L_e, \theta) sin2\theta dL_e d\theta + \int_0^{\frac{\pi}{2}}\int_{l_d(\delta)}^{\frac{L_f}{2}} \sigma_{bd}(\delta, \theta) sin2\theta dL_e d\theta \right. & 0 < \delta \le \delta^* \\ \frac{V_f}{L_f}\int_0^{\frac{\pi}{2}}\int_\delta^{\frac{L_f}{2}} \sigma_{bp}(\delta, L_e, \theta) sin2\theta dL_e d\theta & \delta^* < \delta \le \frac{L_f}{2} \end{cases} \quad [13]$$

4.3. Fiber rupture in debonding stage

Fibers will be fractured when the maximum fiber bridging stress is higher than its apparent tensile strength $(\sigma_{bd}(\delta, \theta)_{max} \ge \sigma_{fu}(\theta))$ during debonding process. Specially, the fiber critical embedment length

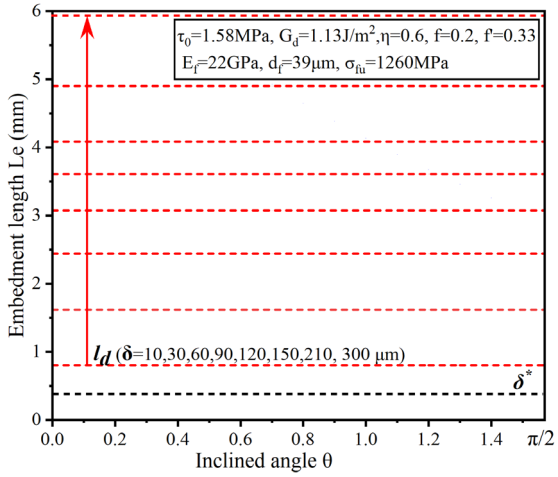

Figure 3. The fiber embedment at full debonding point with a varying crack opening width.

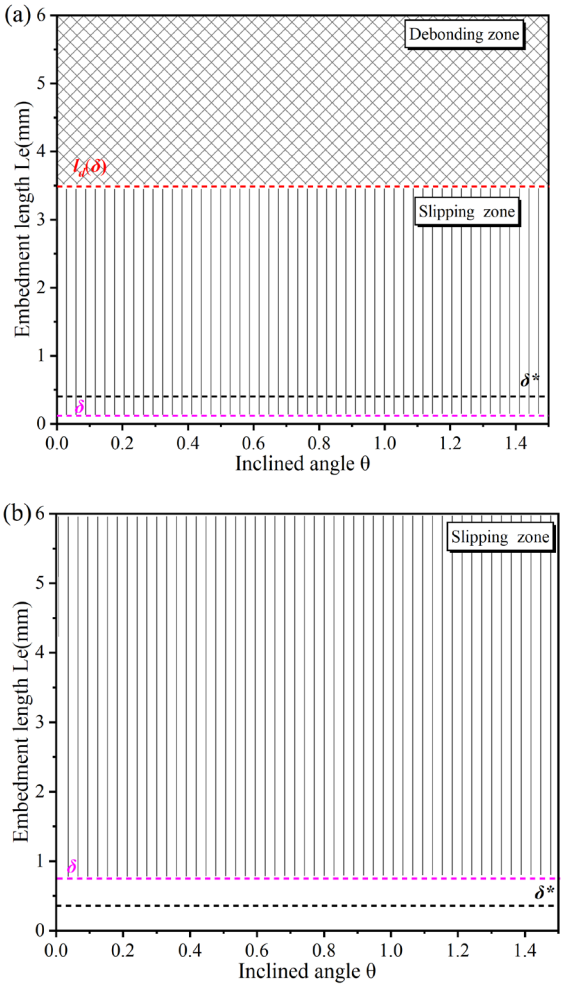

Figure 4. Fiber states without fiber rupture. (a) $0 < \delta \le \delta^*$; (b) $\delta^* < \delta \le \frac{L_f}{2}$.

L_d is derived by making the fiber bridging stress in complete debonding point equal the fiber tensile fracture strength $\sigma_{fu}(\theta)$ (21), as given in Equation [14].

$$L_d(\theta) = \frac{d_f \sigma_{fu}}{4\tau_0} e^{-(f+f')\theta} - \frac{\sqrt{2d_f E_f G_d(1+\eta)}}{2\tau_0} \quad [14]$$

Figure 5 illustrates the fiber critical embedment and debonding rupture zone with varying crack opening width. The fiber embedment increases as the crack opening width increases, which could reach $L_f/2$ when crack opening width is up to δ^*. Moreover, the debonding rupture zone increases with the crack opening width increases up to δ^*. As the crack opening width δ increases, three scenarios could be divided to calculate the fiber bridging stress at debonding rupture zone, as shown in Figure 6. From Figure 6a, when δ lies between 0 and δ^*, three main zones could be classified for all fibers, which include slipping zone (SZ), debonding zone (DZ), and debonding rupture zone (DRZ). Fibers in debonding zone (DZ1) will be fractured under tensile load, while fibers in debonding zone (DZ2) suffer full debonding and slipping process without rupture. Moreover, fibers in debonding rupture zone have fractured, which have reached the embedment length $l_d(\delta)$ at full debonding point.

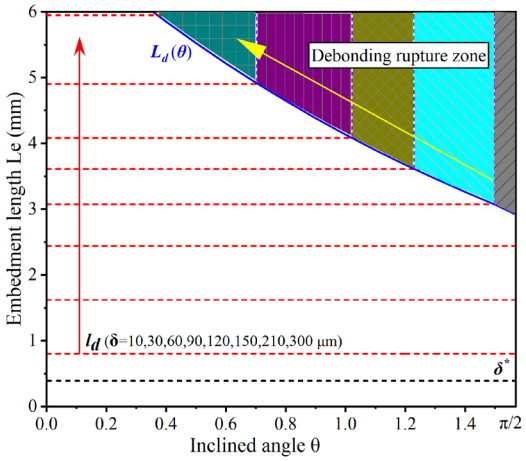

Figure 5. The fiber critical embedment and debonding rupture zone with a varying crack opening width.

θ_d produced by the intersection point between $L_d(\theta)$ and $L_f/2$ can be calculated by Equation [15]. Moreover, θ_c could be derived by making $L_d(\theta)$ be equal to $l_d(\delta)$ (21), as presented in Equation [16] and [17].

$$\theta_d = \begin{cases} \frac{\pi}{2} & \frac{L_f}{2} \le L_d\left(\frac{\pi}{2}\right) \\ -\frac{1}{f+f'} \ln \frac{2L_f\tau_0 + 2\sqrt{2E_f d_f(1+\eta)}}{d_f \sigma_{fu}} & L_d\left(\frac{\pi}{2}\right) \le \frac{L_f}{2} \le L_d(0) \\ 0 & \frac{L_f}{2} > L_d(0) \end{cases} \quad [15]$$

$$\theta_c{}' = -\frac{1}{2(f+f')} \ln \frac{4E_f(1+\eta)}{\sigma_{fu}{}^2 d_f} (\delta\tau_0 + 2G_d) \quad [16]$$

$$\theta_c(\delta) = \begin{cases} \frac{\pi}{2} & \frac{\pi}{2} < \theta_c{}' \\ \theta_c{}' & \theta_d \le \theta_c{}' \le \frac{\pi}{2} \\ \theta_d & \theta_c{}' < \theta_d \end{cases} \quad [17]$$

When δ lies between δ^* and $L_d\left(\frac{\pi}{2}\right)$, the debonding rupture zone (DRZ) and slipping zone (SZ) were presented in Figure 6b. Fibers in DRZ have fractured and reached the embedment length $l_d(\delta)$ at full debonding point. Additionally, Figure 6c shows that the debonding rupture zone of fibers reduces as δ increases from $L_d\left(\frac{\pi}{2}\right)$ to $L_f/2$. The inclined angle $\theta_a(\delta)$ could be calculated by making $L_d(\theta)$ equal δ (21), as defined by Equation [18]. Hence, the fiber rupture bridging stress σ_D in bebonding stage versus the increasing crack opening width δ relation can be evolved by combining the contributory fractured fibers, as given in Equation [19].

4.4. Fiber fracture in slipping stage

Fiber bridging stress can be strengthened since the slip hardening feature of PVA fiber emerges in slipping stage. Hence, fiber slipping fracture also can be presented when the maximum fiber bridging stress $\sigma_{bp}(\delta,\theta)_{max}$ grow higher than the fiber apparent

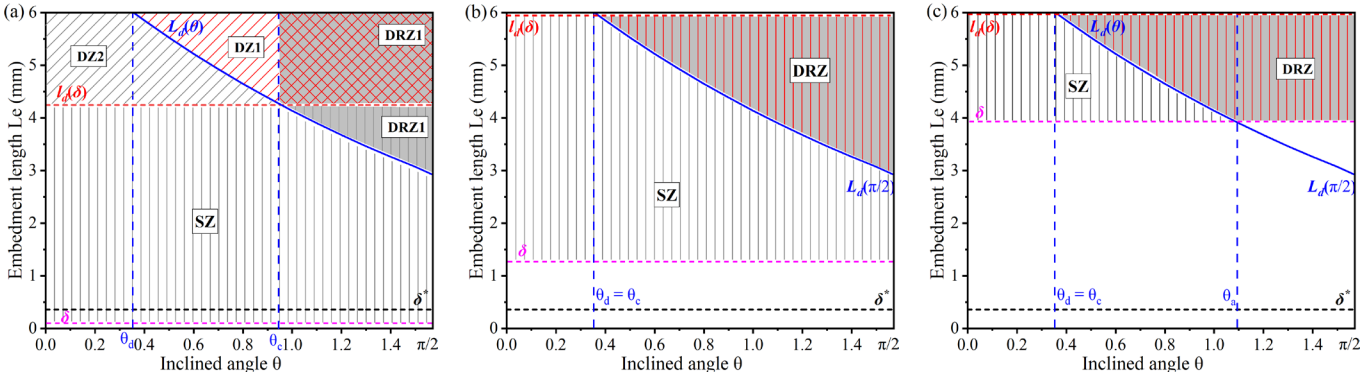

Figure 6. Fiber debonding rupture zone. (a) $0 \le \delta \le \delta^*$; (b) $\delta^* \le \delta \le L_d\left(\frac{\pi}{2}\right)$; (c) $L_d\left(\frac{\pi}{2}\right) \le \delta \le \frac{L_f}{2}$.

tensile strength $\sigma_{fu}(\theta)$. The maximum fiber bridging stress could be deduced by Equation [20], corresponding to $\delta_{max}=\frac{L_e}{2}+2\delta_0+\frac{d_f}{2\beta}$ (33). Furthermore, another fiber critical embedment length $L_p(\theta)$ could be derived by making $\sigma_{bp}(\delta_{max},\theta)$ equal $\sigma_{fu}(\theta)$, as given in Equation [21].

$$\theta_a(\delta)=\begin{cases}\frac{\pi}{2} & 0\le\delta\le L_d\left(\frac{\pi}{2}\right)\\ -\frac{1}{(f+f')}\ln\frac{4\tau_0}{d_f\sigma_{fu}}\left(\delta+\frac{\sqrt{2d_fE_fG_d(1+\eta)}}{2\tau_0}\right) & L_d\left(\frac{\pi}{2}\right)\le\delta\le\frac{L_f}{2}\end{cases} \quad [18]$$

$$\sigma_D(\delta)=\begin{cases}\frac{V_f}{L_f}\begin{cases}\int_{\theta_c(\delta)}^{\frac{\pi}{2}}\int_{l_d(\delta)}^{\frac{L_f}{2}}\sigma_{bd}(\delta,\theta)sin2\theta dL_e d\theta+\\ \int_{\theta_c(\delta)}^{\frac{\pi}{2}}\int_{L_d(\theta)}^{l_d(\delta)}\sigma_{bp}(\delta,L_e,\theta)sin2\theta dL_e d\theta\end{cases} & 0\le\delta\le\delta^*\\ \frac{V_f}{L_f}\int_{\theta_c(\delta)}^{\frac{\pi}{2}}\int_{L_d(\theta)}^{\frac{L_f}{2}}\sigma_{bp}(\delta,L_e,\theta)sin2\theta dL_e d\theta & \delta^*\le\delta\le L_d\left(\frac{\pi}{2}\right)\\ \frac{V_f}{L_f}\begin{cases}\int_{\theta_a(\delta)}^{\frac{\pi}{2}}\int_{\delta}^{\frac{L_f}{2}}\sigma_{bp}(\delta,L_e,\theta)sin2\theta dL_e d\theta\\ \int_{\theta_c(\delta)}^{\theta_a(\delta)}\int_{L_d(\theta)}^{\frac{L_f}{2}}\sigma_{bp}(\delta,L_e,\theta)sin2\theta dL_e d\theta\end{cases} & L_d\left(\frac{\pi}{2}\right)\le\delta\le\frac{L_f}{2}\end{cases} \quad [19]$$

$$\sigma_{bp}(\delta_{max},\theta)=\frac{\tau_0e^{f\theta}}{d_f}\left(\frac{{L_e}^2\beta}{d_f}+2L_e+\frac{d_f}{\beta}\right) \quad [20]$$

$$L_p(\theta)=d_f\left(\sqrt{\frac{\sigma_{fu}e^{-(f+f')\theta}}{\beta\tau_0}}-\frac{1}{\beta}\right) \quad [21]$$

As crack opening width expands, a new critical embedment length $l_p(\delta)$ resulting in fracturing for the slipping fibers can also be derived by letting $\sigma_{bp}(\delta,\theta)$ equal $\sigma_{fu}(\theta$, as shown in Equation [22], indicating that fibers with an embedment length higher than $l_p(\delta)$ has fractured in the current crack opening width (21).

$$l_p(\delta)=\frac{{d_f}^2\sigma_{fu}e^{-(f+f')\theta}}{4\tau_0(d_f+\beta(\delta-2\delta_0))}+(\delta-2\delta_0) \quad [22]$$

Fiber slipping rupture zone is determined by the combined curve of $l_p(\delta)$, $L_p(\theta)$, and $L_d(\theta)$. However, $l_p(\delta)$ is an inapprehensible curve since δ_0 is the quadratic function of L_e. Huang et al. (14) strictly omitted δ_0 in Equation [22]. Actually, an essential δ_0 should be derived to achieve the better prediction accuracy of σ(δ) relation. Hence, a new assuming in this study, embedment length L_e of all fibers conservatively lie between $L_p(\frac{\pi}{2})$ and $L_d(\frac{\pi}{2})$ and presents a random uniform distribution in the slipping rupture zone, which was proposed to identify, and account for the slipping fracture section. Afterward, the probability density function of L_e is proposed to get the average $\delta_{0\,average}$, as defined in Equation [23] and [24]. The revised current critical embedment length $l_p(\delta)$ can be shown as in Equation [25].

$$f(L_e)=\frac{1}{L_d(\frac{\pi}{2})-L_p(\frac{\pi}{2})} \quad [23]$$

$$\delta_{0\,Average}=\int_{L_p(\frac{\pi}{2})}^{L_d(\frac{\pi}{2})}\delta_0(L_e)f(L_e)dL_e \quad [24]$$

$$l_p(\delta)=\frac{{d_f}^2\sigma_{fu}e^{-(f+f')\theta}}{4\tau_0(d_f+\beta(\delta-2\delta_{0\_average}))}+(\delta-2\delta_{0\_average}) \quad [25]$$

Figure 7 illustrates the limiting embedment length at slipping state and slipping rupture zone with varying crack opening distance. The slipping rupture zone gradually increases as crack opening expands. Figure 8 shows the fiber slipping rupture zone. It is noteworthy to see that the slipping rupture zone starts to occur when crack plane expands a minimum width δ_{min} that can be approximately calculated by making $l_p\left(\delta_{min},\frac{\pi}{2}\right)$ equal $L_d\left(\frac{\pi}{2}\right)$ using Equation [26]. Thus, the slipping rupture zone is zero when crack opening width is lower than δ_{min}, as shown in Figure 8a.

$$\frac{{d_f}^2\sigma_{fu}e^{-(f+f')\frac{\pi}{2}}}{4\tau_0(d_f+\beta(\delta_{min}-2\delta_{0\_average}))}+(\delta_{min}-2\delta_{0\_average})=\frac{d_f\sigma_{fu}}{4\tau_0}-\frac{\sqrt{2d_fE_fG_d(1+\eta)}}{2\tau_0} \quad [26]$$

Moreover, the slipping rupture zone increases as the crack plane increases from δ_{min} to δ^* (see Figure 8 b). The inclined angle θ_b could be calculated by letting $l_p(\delta)$ equal $L_f/2$ (21), as given in Equation [27] and [28]. The curve of $l_p(\delta)$ and $L_d(\theta)$ almost coincide when the crack opening width expand to $L_f/16$ (see Figure 8 c). Generally, the crack opening width corresponding to the peak fiber bridging stress is lower than $L_f/16$ (around 750 μm). Hence, the fiber rupture bridging stress σ_S in slipping stage versus increasing crack opening width δ (lower than $L_f/16$) for composites can be deduced by integrating the contributory fractured fibers, as presented in Equation [29].

$${\theta_b}'=-\frac{1}{f+f'}\ln\left[\frac{2\tau_0\left(\beta\left(\delta-2\delta_{0_{average}}\right)+d_f\right)\left(L_f-2\left(\delta-2\delta_{0_{average}}\right)\right)}{\sigma_{fu}d_f^2}\right] \quad [27]$$

$$\theta_b=\begin{cases}0 & {\theta_b}'\le 0\\ {\theta_b}' & {\theta_b}'>0\end{cases} \quad [28]$$

$$\sigma_S(\delta)=\begin{cases}0 & 0\le\delta\le\delta_{min}\\ \frac{V_f}{L_f}\begin{cases}\int_{\theta_b}^{\theta_d}\int_{l_p(\delta,\theta)}^{\frac{L_f}{2}}\sigma_{bp}(\delta,L_e,\theta)sin2\theta dL_e d\theta+\\ \int_{\theta_d}^{\frac{\pi}{2}}\int_{l_p(\delta,\theta)}^{L_d(\theta)}\sigma_{bp}(\delta,L_e,\theta)sin2\theta dL_e d\theta\end{cases} & \delta_{min}\le\delta\le\frac{L_f}{16}\end{cases} \quad [29]$$

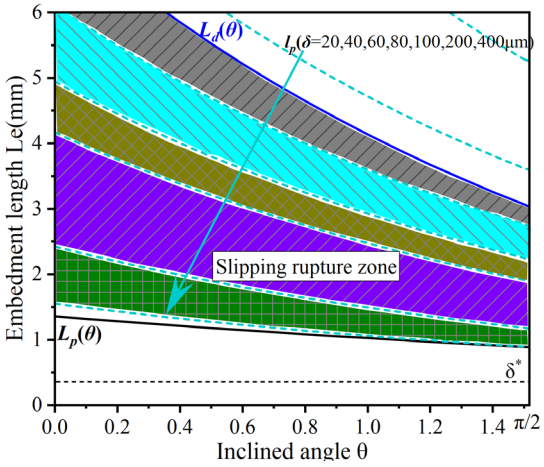

Figure 7. The limiting embedment length in slipping stage and slipping rupture zone with varying crack opening distance.

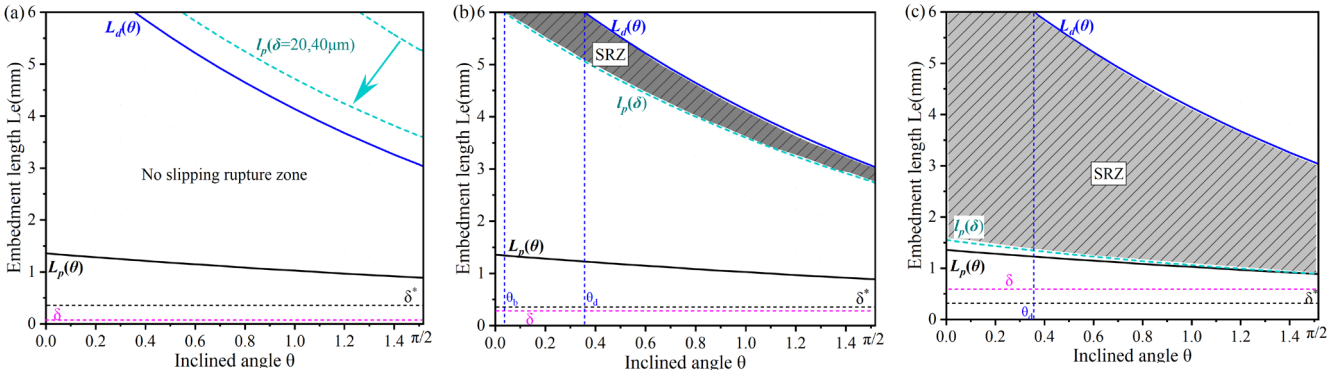

Figure 8. Fiber slipping rupture zone. (a) ; (b); (c).

4.5. Effective fiber bridging stress

On basis of above derivation, the fiber bridging stress without fiber fracture deducts the fiber debonding and slipping rupture stress, thus derivating the effective fiber bridging stress of composites, as presented in Equation [30].

$$\sigma_{effective}(\delta) = \sigma_N(\delta) - \sigma_D(\delta) - \sigma_S(\delta) \qquad [30]$$

5. FIBER TWO-WAY PULLOUT CONSIDERATION

Fiber two way pullout was first reported with respect to PVA fiber due to slip-hardening interface behavior (34). The $\sigma_{effective}(\delta)$ exclude the fiber two-way pullout situation. In this study, the so-called nominal fiber was adopted to supply a reasonably approximate crack opening width contributed by fiber two-way pullout (14, 23).

The single fiber bridging stress is the function of embedment length L_e and inclined angle θ, thus Equation (10) can be rewritten as Equation [31] (23) Where ξ_b is the efficiency of fiber bridging, which represents the fiber contributing stress as fibers increasingly fracture across a crack plane. Thus, ξ_b will gradually reduce to zero. It is noteworthy that the efficiency fiber contributing stress for fibers containing the rupture fiber in debonding and slipping stage is defined as $\xi_{effective_b}$ which is given in Appendix I. Hence, according to Equation [31], σ_b is presented in Equation [33]. For fibers having a long embedment length l_e ($l_e \in (\frac{L_f}{2}, L_f)$), under the effective bridging stress σ_b, the displacement of fiber in debonding and pullout stage can be deduced (14), as given in Equation [34] and [35], respectively.

$$\sigma(\delta) = \frac{V_f}{L_f}\int_0^{\frac{\pi}{2}}\int_0^{\frac{L_f}{2}} \sigma_b(\delta, L_e, \theta) sin2\theta dL_e d\theta = \qquad [31]$$

$$\sigma_b \quad \frac{V_f}{L_f}\int_0^{\frac{\pi}{2}}\int_0^{\frac{L_f}{2}} sin2\theta dL_e d\theta = \sigma_b \; V_f \xi_b$$

Where σ_b is the nominal fiber bridging stress, ξ_b can be derived in Equation [32].

$$\xi_b = \frac{1}{L_f}\int_0^{\frac{\pi}{2}}\int_0^{\frac{L_f}{2}} sin2\theta dL_e d\theta \quad [32]$$

$$\sigma_b = \frac{\sigma_{effective}(\delta)}{V_f \xi_{effective_b}} \quad [33]$$

$$(\delta) = \frac{V_f}{L_f}\int_0^{\frac{\pi}{2}}\int_0^{\frac{L_f}{2}} \sigma_b(\delta, L_e, \theta) sin2\theta dL_e d\theta = \sigma_b \ \frac{V_f}{L_f}\int_0^{\frac{\pi}{2}}\int_0^{\frac{L_f}{2}} sin2\theta dL_e d\theta = \sigma_b \ V_f \xi_b \quad [33]$$

$$\delta_{L,d} = \left[\left(\frac{\sigma_b V_f}{4\sigma_0}\right)^2 - \frac{\gamma^2}{4}\right] u_0 \qquad \sigma_b \le \frac{4\sigma_0}{V_f}\left(\frac{l_e}{\frac{L_f}{2}} + \frac{\gamma}{2}\right) [34]$$

$$\delta_{L,p} = \frac{L_f}{4}\left(\frac{l_e}{\frac{L_f}{2}} - \alpha\right) - \frac{L_f}{2}\sqrt{\frac{1}{4}\left(\frac{l_e}{\frac{L_f}{2}} - \alpha\right)^2 - \frac{\alpha V_f \sigma_b}{4\sigma_0}} \qquad \frac{4\sigma_0}{V_f}\left(\frac{l_e}{\frac{L_f}{2}} + \frac{\gamma}{2}\right) \le \sigma_b \quad [35]$$

Where $\sigma_0 = \frac{\tau_0 V_f L_f}{2d_f}, \gamma = \frac{\sqrt{8G_d E_f d_f (1+\eta)}}{\tau_0 L_f}, u_0 = \frac{\tau_0 {L_f}^2}{E_f d_f (1+\eta)}, \alpha = \frac{2d_f}{\beta L_f}$. The displacement of δ_L is the function of maximum fiber bridging stress $\sigma_{b_{max}}$ and embedment length of the long side l_e in the loading process, as shown in Equation [36].

$$\delta_L = \delta_L(\sigma_{b_{max}}, l_e) \quad [36]$$

Assuming l_e is a uniform random distribution in the interval from $\frac{L_f}{2}$ to L_f, thus the probability density function of l_e is defined as $f(l_e)$ by Equation [37]. Afterwards, the remedial crack opening width δ_r is approximately averaging δ_L by the integral of l_e, as presented in Equation [38].

$$f(l_e) = \frac{1}{L_f - L_f/2} = \frac{2}{L_f} \quad l_e \in \left(\frac{L_f}{2}, L_f\right) \quad [37]$$

$$\delta_r = \int_{L_f/2}^{L_f} \delta_L(\sigma_{b_{max}}, l_e) f(l_e) dl_e \quad [38]$$

Moreover, it is known from Equation [34], the maximum fiber bridging stress $\sigma_{b_{max}}$ in debonding stage has a critical value (see Equation [39]), which deduces the current fiber critical embedment length l_{e0}, as given in Equation [40].

$$\sigma_{b_{max}} \le \frac{4\sigma_0}{V_f}\left(\frac{l_e}{\frac{L_f}{2}} + \frac{\gamma}{2}\right) \quad [39]$$

$$l_{e0} = \frac{L_f}{2}\left(\frac{V_f \sigma_{b_{max}}}{4\sigma_0} - \frac{\gamma}{2}\right) = \frac{L_f}{2}\left(\zeta - \frac{\gamma}{2}\right) \quad [40]$$

Where $\zeta = \frac{V_f \sigma_{b_{max}}}{4\sigma_0}$. A long embedment length of fibers with higher than l_{e0} is still at the debonding stage.

According to the above definition, two scenarios could be generated according to l_{e0}.If $l_{e0} \le \frac{L_f}{2}$ namely $\sigma_{b_{max}} \le \frac{4\sigma_0}{V_f}\left(1 + \frac{\gamma}{2}\right)$, implying that the long embedded side of fibers is in debonding process, δ_r is given by Huang et al. (14).

$$\delta_r = \int_{\frac{L_f}{2}}^{L_f} \delta_{L,d}(\sigma_{b_{max}}) f(l_e) dl_e \ = \left(\zeta^2 - \frac{\gamma^2}{4}\right) u_0 \quad [41]$$

If $\frac{L_f}{2} < l_{e0} \le L_f$, namely $\frac{4\sigma_0}{V_f}\left(1 + \frac{\gamma}{2}\right) \le \sigma_{b_{max}} < \frac{4\sigma_0}{V_f}\left(2 + \frac{\gamma}{2}\right)$, which indicates that the long embedded side of fibers is in the debonding and pullout process, δ_r is given as follows [42]:

$$\delta_r = \int_{\frac{L_f}{2}}^{l_{e0}} \delta_{L,p}(\sigma_{b_{max}}, l_e) f(l_e) dl_e + \int_{l_{e0}}^{L_f} \delta_{L,d}(\sigma_{b_{max}}) f(l_e) dl_e = \left(\zeta^2 - \frac{\gamma^2}{4}\right)\left(2 - \zeta + \frac{\gamma}{2}\right) u_0 + \frac{L_f}{4}\left[\frac{1}{2}(\zeta - \frac{\gamma}{2})^2 - \alpha(\zeta - \frac{\gamma}{2})\right] - \frac{L_f}{4}\left(\frac{1}{2} - \alpha\right) - \frac{2L_f\left[\frac{1}{4}\left(\zeta - \frac{\gamma}{2} + \alpha\right)^2 - \alpha\zeta\right]^{\frac{3}{2}}}{3\left(\zeta - \frac{\gamma}{2} + \alpha\right)} + \frac{2L_f\left[\frac{1}{4}(1+\alpha)^2 - \alpha\zeta\right]^{\frac{3}{2}}}{3(1+\alpha)} \quad [42]$$

6. COOK-GORDON EFFECT

Cook-Gordon effect will contribute the additional width to the $\sigma_{effective}(\delta)$, which describes a precocious fiber debonding normal process. Meanwhile, the fiber-matrix is separated under the fiber bridging stress related to the elastic crack tip field of the adjoining matrix crack in the horizontal plane, thus leading to an attached crack opening δ_{cg} generated from the fiber elastic stretching of the fiber segment (23). Therefore, the fiber debonding process initiates ahead of the matrix cracking, leading to stretch a free fiber segment δ_{cg}, as given in Equation [43] (23).

$$\delta_{cg} = \frac{\alpha \sigma_{effective}(\delta)}{V_f E_f \xi_{effective_b}} \quad [43]$$

Where α is the Cook-Gordon parameter. In general, $\alpha = 2d_f$ for PVA fiber was suggested, while α is set as 15 for polyethylene (PE), and polypropylene (PP) fibers (35).

Overall, the total crack opening width including the contribution of fiber two-way pullout and Cook-Gordon effect is given as [44]:

$$\delta = \delta + \delta_r + \ \delta_{cg} \quad [44]$$

7. MODEL VALIDATION

Figure 9 shows the computation flow scheme of final $\sigma(\delta)$. The experimental data including fiber, matrix, and fiber/matrix parameters from Yang et al. (23) were employed to verify the final $\sigma(\delta)$. The micro-parameters for PE-ECC and PVA-ECC are listed in Table 1. It is well known that PVA fiber has a strong chemical bond strength and slip hardening behavior in hardened pastes. Table 1 illustrates the micro-parameters for PVA-ECC and PE-ECC.

Figure 10 shows theoretical $\sigma(\delta)$ relation of PVA-ECC analyzed by the current model. When only one way was considered, the predicted peak bridging stress and corresponding crack opening width were 64 μm and 1.50 MPa, respectively. If two ways are accounted, the same peak stress is obtained at the crack opening width of 165.8 μm. Moreover, the Cool-Gordon effect can add 2.1 μm to the crack opening width and reach 167.9 μm, indicating that the contribution of Cool-Gordon effect to crack opening width is faint due to the small assuming Cook-Gordon parameter $\alpha = 2d_f$ for PVA fiber.

Figure 11 illustrates the predicted composite $\sigma - \delta$ relation of PVA-ECC. The predicted and experimental composite characteristics of PVA-ECCs and PE-ECCs are listed in Table 2. From Figure 11, it was difficult to research the variation of pseudo elastic properties of three models in the elastic part. The approximate first crack strength from three models was presented, which was lower than the experimental data. Afterward, cracks gradually develop during strain in three models, which show a different maximum fiber bridging stress and corresponding crack opening width. Moreover, the accuracy coefficients of the two key parameters by three models are listed in Table 2. For PVA-ECC with a volume fraction of 0.1%, the experimental curves scattered inside the grey zone referenced by (23), where its peak stress and corresponding crack opening width was 0.295 MPa and 165.0 μm, respectively, while that of Huang et al. (14) presented a peak stress of 0.31 MPa at the crack width of 131.0 μm, and that of Yang et al. (23) has a peak stress of 0.35 Mpa at the crack width of 107.0 μm. Hence, employing the current model could further improve the accuracy of crack opening width that reaches 175.1μm with a proximal peak bridging stress of 3.0 MPa. In addition, for PVA-ECC with a volume fraction of 0.5 %, the maximum fiber bridging stress obtained by Huang's model, Yang's model, and the current model were 1.52 MPa, 1.72 MPa, and 1.50 MPa, respectively, while the corresponding crack opening width were 141.5μm, 125.6 μm, and 171.9 μm, respectively. Hence, compared to the real experimental maximum fiber bridging stress of 1.65MPa and crack opening width of 160.1 μm, the current model has a higher prediction accuracy than the other two models (see Table 2). It was clearly found that a proximate crack opening presented higher precision by using the current model than the other two predicted models. In fact, the current models use the opposite logic calculation compared to the Huang's model, in which fiber bridging stress with no rupture subtracts the fiber fracture stress in debonding and pullout stage. In Huang's model, the operative partial fiber bridging stress in the debonding and pullout stage are severalty picked, thereafter summing those partial stresses to form the fiber bridging stress of composites. Therefore, the current model provides an effective accuracy compared to the experimental data, which is also easy to understand for researchers focusing on the fiber reinforced cement composites field.

Table 1. The micro-parameters for PVA-ECC and PE-ECC.

Types	PVA-ECC (23)		PE-ECC (37)				
-			-	M-C	M-25	M-50	M-100
Fiber	d_f (mm)	39	d_f (mm)	26	26	26	26
	L_f (mm)	12	L_f (mm)	18	18	18	18
	E_f (GPa)	22	E_f (GPa)	120	120	120	120
	σ_{fu} (MPa)	1060	σ_{fu} (MPa)	3000	3000	3000	3000
	f'	0.33	f'	0.33	0.33	0.33	0.33
	V_f (%)	0.01/0.05	V_f (%)	0.2	0.2	0.2	0.2
Matrix	E_m (GPa)	20	E_m (GPa)	20.4	36.3	38.8	32.1
Interface	τ_0 (MPa)	1.58	τ_0 (MPa)	1.53	2.41	2.308	2.85
	G_d (J/m^2)	1.13	G_d (J/m^2)	0	0	0	0
	β	0.6	β	0.0063	0.0090	0.0063	0.0050
	f	0.2	f	0.59	0.59	0.59	0.59

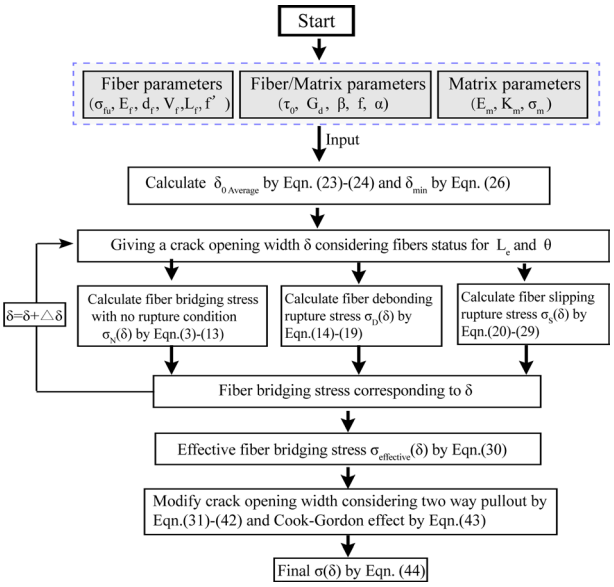

Figure 9. Computation flow chart of final σ(δ).

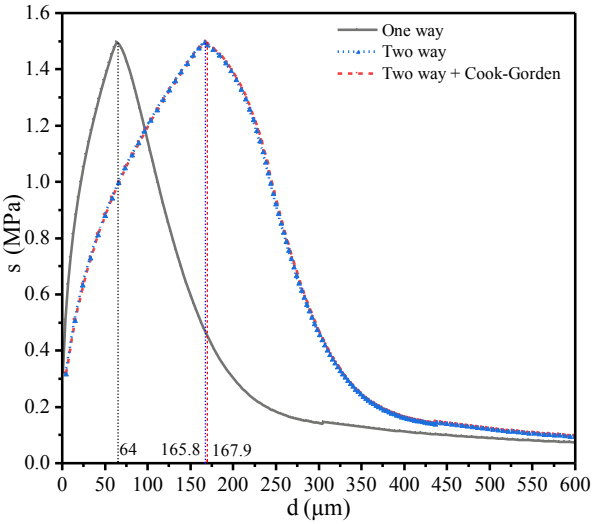

Figure 10. Theoretical relation of PVA-ECC analyzed by three models.

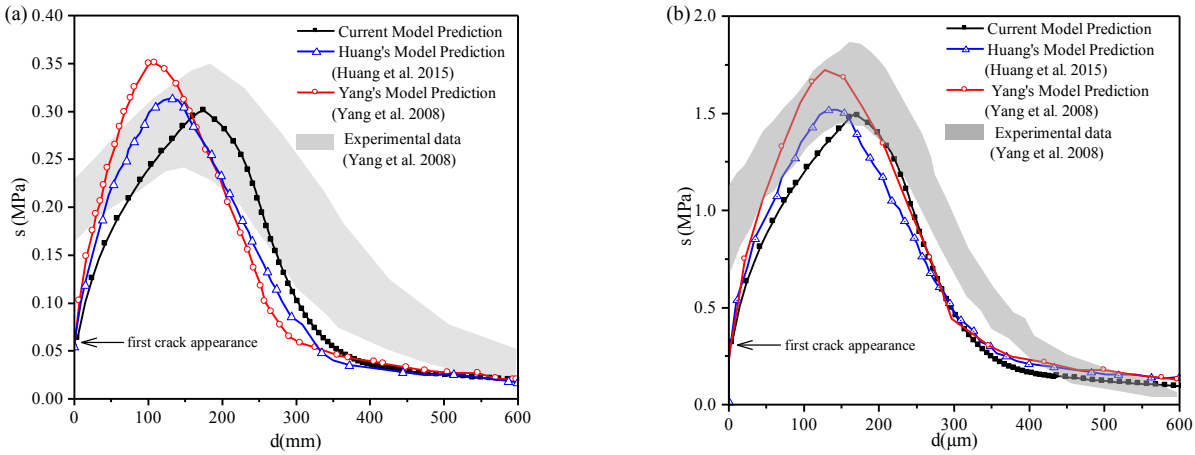

Figure 11. Comparison of predicted and experimental σ − δ relation of PVA-ECC: (a) 0.1% and (b) 0.5% by volume.

Based on the micro-parameters in the previous study (36), Figure 12 demonstrates the comparison of the predicted σ − δ relation for PE-ECC by three models. It can be seen from Figure 12 and Table 2 that, the maximum bridging stress and corresponding crack opening width of the M-C group by using Yang's model are around 12.99 MPa and 99.0 μm, respectively, while that of Huang's model presented a maximum stress of 13.1 Mpa at the crack width of 56.8 μm. Noticeably, the Cool-Gordon effect was significant in verifying the real width of PE-ECC due to the big Cool-Gordon effect of $\alpha = 15\ d_f$, which was not included in Huang's model from Figure 12 (b), (c) and (d). Employing the current model could further improve this accuracy of crack opening width that reaches 97.9 μm with a slightly bigger peak bridging stress of 14.0 MPa. Hence, Yang's model and the current model have a higher average crack width than Huang's model for PE-ECC since the Cool-Gordon effect of Huang's model could not effectively be implemented. On the other hand, Yang's model and current model show a proximal value for M-25, M-50, and M-100 compared to the real average crack width calculated from the crack patterns of the tensile test. A near-peak bridging stress was illustrated for three models. However, the current model is easy to calculate compared to the implicit Yang's model. However, the corresponding crack opening width at maximum bridging stress by three models is lower than the experimental data for PE-ECC since there is amount of inelastic strain produced by micro-cracks near the main crack (15).

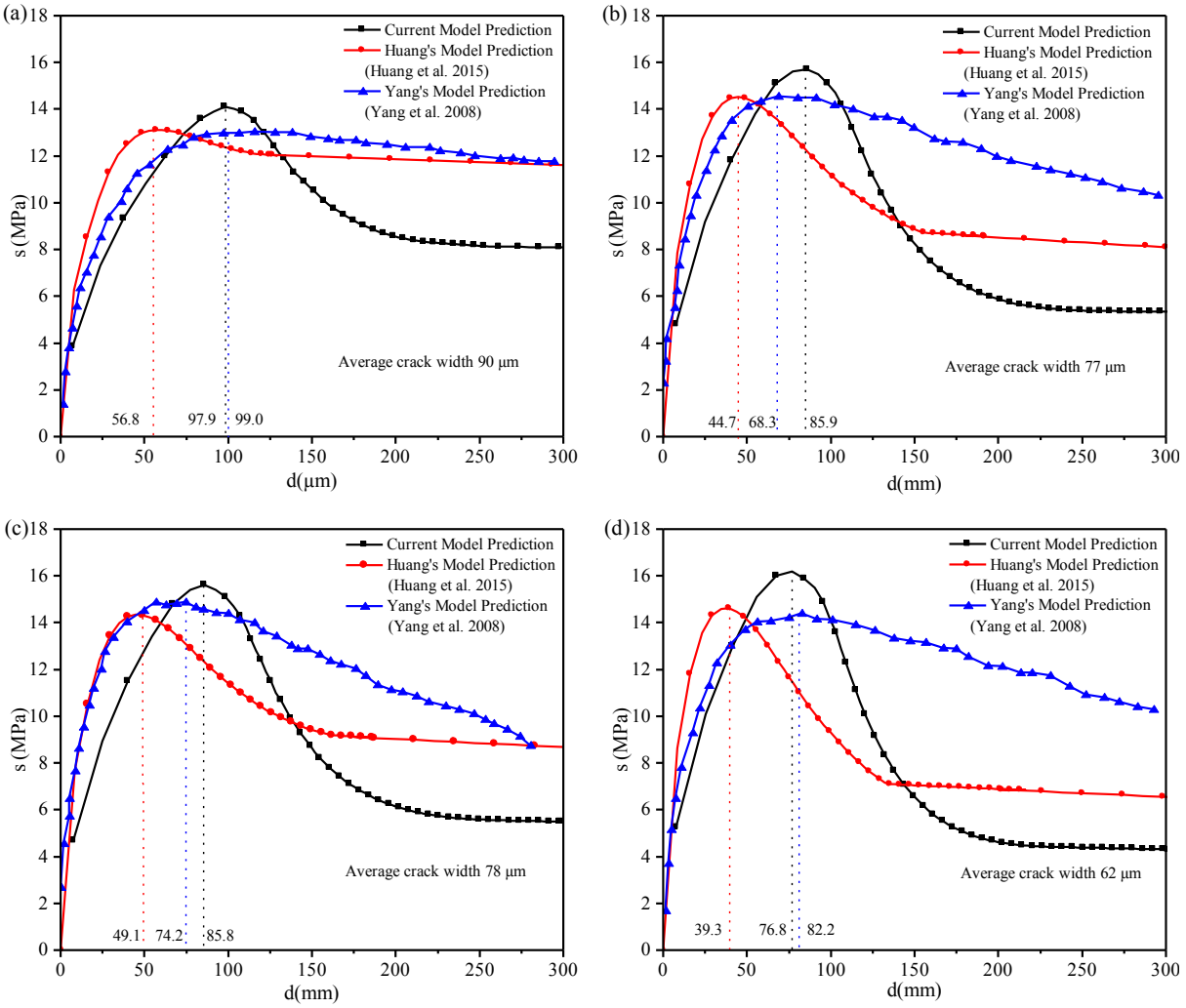

Figure 12. Comparison of predicted σ − δ relation for PE-ECC by three models.

Table 2. Predicted and experimental composite characteristics of PVA-ECCs and PE-ECCs.

Model	Parameter	PVA-ECC (23)		PE-ECC (37)			
		0.1%[a] (Accuracy coefficients)	0.5% [a] (Accuracy coefficients)	M-C	M-25	M-50	M-100
Experiment	σ_{peak_mean} (MPa)[b]	0.295	1.65	—	—	—	—
	δ_{mean} (μm)	165.0	160.1	—	—	—	—
Current model	σ_{peak} (MPa)	0.3 (+1.7%)	1.50 (-9.1%)	14.1	15.7	15.6	16.2
	δ_{mean} (μm)	175.1 (+6%)	171.9 (+7.3)	97.9	85.9	85.8	76.8
Model of Huang et al.	σ_{peak} (MPa)	0.31 (+5.1%)	1.52 (-7.8%)	13.1	14.5	14.3	14.6
	δ_{mean} (μm)	131.0 (-20.6%)	141.5 (-11.6%)	56.8	44.7	49.1	39.3
Model of Yang et al.	σ_{peak} (MPa)	0.35 (+18.5%)	1.72 (+4.2%)	12.99	14.5	14.8	14.3
	δ_{mean} (μm)	107.0 (-35.1%)	125.6 (-21.5%)	99.0	68.3	76.2	86.2

[a]: 0.1% and 0.5% represent the volume fraction of PVA fibers.
[b]: σ_{peak_mean} is the mean peak stress of σ(δ) curve from experimental data.

8. CONCLUSIONS

This crack bridging model for ECC was developed with an opposed calculation program based on FPRM model (21), which improves the predicted precision by subtracting the fiber rupture stress in debonding and pullout stage. Based on the results obtained, the following conclusions can be drawn.

(1) From the model validation, the current model was suitable to PVA-ECC due to the slip hardening property of PVA fiber, while the fiber two-way pullout is most responsible for improving the correction prediction of the crack opening, yet Cook-Gordon presents a faint effect on the crack width. Moreover, compared to Huang's model and Yang's model, the current model presented a higher prediction accuracy for the crack opening width at the maximum fiber bridging stress for PVA-ECC due to the consideration of average δ_0 in embedment length of the fiber.

(2) For PE-ECC, the Cook-Gordon effect could not be neglected due to its bigger Cook-Gordon effect parameters. The crack opening width obtained from Huang's model was notably lower than that of Yang's model and the current model since the Cook-Gordon effect could not be enforced in Huang's model. (3) To sum up, the fiber bridging stress vs crack opening width relation obtained by the current explicit fiber bridging model presented a greater accuracy than the other two models. Importantly, the current model can help ECC micromechanics-based material design theory, and the calculating procedure was easy to understand for researchers.

Funding sources

Research carried out within the framework of Project (Grant No. 51678379) financed by the National Natural Science Foundation of China and Key Research and Development Program of Sichuan province (2023YFQ0047) for the financial support of this work.

Authorship contribution statement

Zhiwen Wang: Conceptualization, Data cleansing, Formal analysis, Research, Methodology, Software, Visualization, Writing – original draft, Writing – review & editing

Bixiong Li: Fund raising, Project administration, Resources, Supervision

Lianghui Li: Research, Visualization

Zhibo Zhang: Research, Visualization

Declaration of competing interest

The authors of this article declare that they have no financial, professional or personal conflicts of interest that could have inappropriately influenced this work.

REFERENCES

1. Lu C, Li VC, Leung CKY. 2018. Flaw characterization and correlation with cracking strength in Engineered Cementitious Composites (ECC). Cem. Concr. Res. 107:64-74. https://doi.org/10.1016/j.cemconres.2018.02.024.
2. Liao Q, Su YR, Yu JT, Yu KQ. 2022. Torsional behavior of BFRP bars reinforced engineered cementitious composites beams without stirrup. Eng. Struct. 268:114748. https://doi.org/10.1016/j.engstruct.2022.114748.
3. Li VC, Mishra DK, Wu HC. 1995. Matrix design for pseudo-strain-hardening fibre reinforced cementitious composites. Mater. Struct. 28(184):586-595. https://doi.org/10.1007/BF02473191.
4. Li VC, Wang SX, Wu C. 2001. Tensile strain-hardening behaviorof polyvinyl alcohol engineered cementitious composite (PVA-ECC). ACI Mater. J. 98(6):483-492. https://doi.org/10.1089/apc.2006.20.829.
5. Li M, Li VC. 2011. High-early-strength engineered cementitious composites for fast, durable concrete repair-material properties. ACI Mater. J. 108(1): 3-12. https://doi.org/10.14359/51664210.
6. Liao Q, Yu JT, Xie X, Ye J, Jiang F. 2022. Experimental study of reinforced UHDC-UHPC panels under close-in blast loading. J. Build. Eng. 46:103498. https://doi.org/10.1016/j.jobe.2021.103498.
7. Dupont D, Vandewalle L. 2005. Distribution of steel fibres in rectangular sections. Cem. Concr. Compos. 27(3):391-398. https://doi.org/10.1016/j.cemconcomp.2004.03.005.
8. Barr BIG, Lee MK, Hansen EJDP, Dupont D, Erdem E, Schaerlaekens S, Schnütgen B, Stang H, Vandewalle L. 2003. Round-robin analysis of the RILEM TC 162-TDF beam-bending test: Part 3-Fibre distribution. Mater. Struct. 36(9):631-635. https://doi.org/10.1007/BF02483283.
9. Barr BIG, Lee MK, Hansen EJDP, Dupont D, Erdem E, Schaerlaekens S, Schnütgen B, Stang H, Vandewalle L.. 2003. Round-robin analysis of the RILEM TC 162-TDF uniaxial tensile test: Part 2. Mater. Struct. 36(4):275-280. https://doi.org/10.1007/BF02479621.
10. Li VC, Wu HC. 1992. Conditions for pseudo strain-hardening infiber reinforced brittle matrix composites. J. Appl. Mech. Rev. 45(8):390–398. https://doi.org/10.1115/1.3119767.
11. Zhu B, Pan JL, Zhang M, Leung CKY. 2022. Predicting the strain-hardening behaviour of polyethylene fibre reinforced engineered cementitious composites accounting for fibre-matrix interaction. Cem. Concr. Compos. 134:104770. https://doi.org/10.1016/j.cemconcomp.2022.104770.
12. Kanda T, Lin Z, Li VC. 2000. Tensile stress-strain modeling of pseudostrain hardening cementitious composites. J. Mater. Civ. Eng. 12(2):147–156. https://doi.org/10.1061/(ASCE)0899-1561(2000)12:2(147)
13. Kanda T, Li VC. 2006. Practical design criteria for saturated pseudo strain hardening behavior in ECC. J. Adv. Concr. Technol. 4(1):59-72. https://doi.org/10.3151/jact.4.59.
14. Huang T, Zhang YX, Su C, Lo SR. 2015. Effect of slip-hardening interface behavior on fiber rupture and crack bridging in fiber-reinforced cementitious composites. J. Eng. Mech. 141(10):04015035. https://doi.org/10.1061/(ASCE)EM.1943-7889.0000932.
15. Curosu I, Muja E, Ismailov M, Ahmed AH, Liebscher M, Mechtcherine V. 2021. An experimental-analytical scale-linking study on the crack-bridging mechanisms in different types of SHCC in dependence on fiber orientation. Cem. Concr. Res. 152:106650. https://doi.org/10.1016/j.cemconres.2021.106650.
16. Yao J, Leung CKY. 2020. Scaling up modeling of strain-hardening cementitious composites based on beam theory: From single fiber to composite. Cem. Concr. Compos. 108:103534. https://doi.org/10.1016/j.cemconcomp.2020.103534.
17. Li VC, Leung CKY. 1992. Steady-state and multiple cracking of short random fiber composites. J. Eng. Mech. 118(11):2246-2264. https://doi.org/10.1061/(ASCE)0733-9399(1992)118:11(2246).
18. Zhong L, Li VC. 1997. Crack bridging in fiber reinforced cementitious composites with slip-hardening interfaces. J. Mech. Phys. Solids. 45(5):763-787. https://doi.org/10.1016/S0022-5096(96)00095-6.

19. Maalej M, Li VC, Hashida T. 1995. Effect of fiber rupture on tensile properties of short fiber composites. J. Eng. Mech. 121(8):903-913. https://doi.org/10.1061/(ASCE)0733-9399(1995)121:8(903)
20. Kanda T, Li VC. 1999. Effect of fiber strength and fiber-matrix interface on crack bridging in cement composites. J. Eng. Mech. 125(3):290–299. https://doi.org/10.1061/(ASCE)0733-9399(1999)125:3(290).
21. Lin Z, Kanda T, Li VC. 1999. On interface property characterization and performance of fiber reinforced cementitious composites. J. Adv. Concr. Technol. 1(3):173–184. Retrieved from http://hdl.handle.net/2027.42/84718.
22. Li VC, Wu C, Wang S, Ogawa A, Saito T. 2002. Interface-tailoring for strain-hardening polyvinyl alcohol-engineered cementi tious composite (PVA-ECC). ACI Mater. J. 99(5):463–472. Retrieved from https://acemrl.engin.umich.edu/wp-content/uploads/sites/412/2018/10/Interface-Tailoring-for-Strain-hardening-PVA-ECC.pdf.
23. Yang EH, Wang S, Yang Y, Li VC. 2008. Fiber-bridging constitutive law of engineered cementitious composites. J. Adv. Concr. Technol. 6(1):181-193. https://doi.org/10.3151/jact.6.181.
24. Yu J, Chen YX, Leung CKY. 2018. Micromechanical modeling of crack-bridging relations of hybrid-fiber strain-hardening cementitious composites considering interaction between different fibers. Constr. Build. Mater. 182:629-636. https://doi.org/10.1016/j.conbuildmat.2018.06.115.
25. Kanda T. 1999. New micromechanics design theory for pseudo strain hardening cementitious composite. J. Eng. Mech. 125:373–381. https://doi.org/10.1061/(ASCE)0733-9399(1999)125:4(373).
26. Li VC, Wang SX. 2006. Microstructure variability and macroscopic composite properties of high performance fiber reinforced cementitious composites. Probab. Eng. Eng. Mech. 21(3):201-206. https://doi.org/10.1016/j.probengmech.2005.10.008.
27. Marshall DBAC, COX BN. 1988. A J-integral method for calculating steady-state matrix cracking stresses in composites. Mech. Mater. 7(2):127-133. https://doi.org/10.1016/0167-6636(88)90011-7.
28. ASTM E1820. 2008. Standard test method for measurement of fracture toughness. ASTM International, West Conshohocken, PA, USA.
29. Li VC, Kanda T. 1998. Multiple cracking sequence and saturation in fiber reinforced cementitious composites. Concr. Res. Technol. 9:19–33. https://doi.org/10.3151/crt1990.9.2_19.
30. Li VC, Wang Y, Backer S. 1990. Effect of inclining angle, bundling and surface treatment on synthetic fibre pull-out from a cement matrix. Composites. 21(2):132-140. https://doi.org/10.1016/0010-4361(90)90005-H.
31. Tetsushi K, Li VC. 1992. Multiple cracking sequence and saturation in fiber reinforced cementitious composites. J. Adv. Concr. Technol. 9(2):19-33. https://doi.org/10.3151/crt1990.9.2_19.
32. Li VC, Wang YJ, Backer S. 1991. A micromechanical model of tension-softening and bridging toughening of short random fiber reinforced nrittle matrix composites. J. Mech. Phys. Solids. 39(5):607-625. http://doi.org/10.1016/0022-5096(91)90043-N.
33. Wu C. 2001. Micromechanical tailoring of PVA-ECC for structural applications. University of Michigan.
34. Wang YJ, Li VC, Backer S. 1988. Modelling of fibre pull-out from a cement matrix. Int. J. Cement. Compos. Lightweight. Concr. 10(3):143-149. Retrieved from https://deepblue.lib.umich.edu/bitstream/handle/2027.42/84694/ywang_CCLC88.pdf?sequence=1.
35. Li VC. 1993. From micromechanics to structural engineering. The design of cementitous composites for civil engineering applications. Structural engineering/earthquake engineering. 1993(471):1-12. https://doi.org/10.2208/jscej.1993.471_1.
36. Zhang ZG, Yang Y, Liu JC, Wanga S. 2020. Eco-friendly high strength, high ductility engineered cementitious composites (ECC) with substitution of fly ash by rice husk ash. Cem. Concr. Res 137:106200. https://doi.org/10.1016/j.cemconres.2020.106200.

Appendix

$$\xi_N(\delta) = \begin{cases} \frac{1}{L_f}\left\{\int_0^{\frac{\pi}{2}}\int_{\delta_r}^{l_d(\delta_r)} sin2\theta dL_e d\theta + \int_0^{\frac{\pi}{2}}\int_{l_d(\delta_r)}^{\frac{L_f}{2}} sin2\theta dL_e d\theta\right. & 0 < \delta_r \le \delta^* \\ \frac{1}{L_f}\int_0^{\frac{\pi}{2}}\int_{\delta_r}^{\frac{L_f}{2}} sin2\theta dL_e d\theta & \delta^* < \delta_r \le \frac{L_f}{2} \end{cases} \quad [45]$$

$$\xi_D(\delta) = \begin{cases} \frac{1}{L_f}\left\{\int_{\theta_c(\delta_r)}^{\frac{\pi}{2}}\int_{l_d(\delta_r)}^{\frac{L_f}{2}} sin2\theta dL_e d\theta + \int_{\theta_c(\delta_r)}^{\frac{\pi}{2}}\int_{L_d(\theta)}^{l_d(\delta_r)} sin2\theta dL_e d\theta\right. & 0 \le \delta_r \le \delta^* \\ \frac{1}{L_f}\int_{\theta_c(\delta_r)}^{\frac{\pi}{2}}\int_{L_d(\theta)}^{\frac{L_f}{2}} sin2\theta dL_e d\theta & \delta^* \le \delta_r \le L_d\left(\frac{\pi}{2}\right) \\ \frac{1}{L_f}\left\{\int_{\theta_{d\delta}(\delta_r)}^{\frac{\pi}{2}}\int_{\delta_r}^{\frac{L_f}{2}} sin2\theta dL_e d\theta + \int_{\theta_c(\delta_r)}^{\theta_{d\delta}(\delta_r)}\int_{L_d(\theta)}^{\frac{L_f}{2}} sin2\theta dL_e d\theta\right. & L_d\left(\frac{\pi}{2}\right) \le \delta_r \le L_d\left(\frac{L_f}{2}\right) \end{cases} \quad [46]$$

$$\xi_S(\delta) = \begin{cases} 0 & 0 \le \delta \le \delta_{min} \\ \dfrac{V_f}{L_f}\left\{\displaystyle\int_{\theta_b}^{\theta_d}\int_{l_p(\delta,\theta)}^{\frac{L_f}{2}} sin2\theta dL_e d\theta + \int_{\theta_d}^{\frac{\pi}{2}}\int_{l_p(\delta,\theta)}^{L_d(\theta)} sin2\theta dL_e d\theta\right\} & \delta_{min} \le \delta \le \dfrac{L_f}{16} \end{cases} \quad [47]$$

$$\xi_{effective_b} = \xi_N(\delta) - \xi_D(\delta) - \xi_S(\delta) \quad [48]$$